Supplementary Information File
Excited State Energy Landscape of Phosphorescent Group 14 Complexes

Philipp P. Sikora,[1] Robert Naumann,[1] Christoph Förster[1]* and Katja Heinze[1]*

[1] Department of Chemistry, Johannes Gutenberg University of Mainz, Duesbergweg 10-14, 55128 Mainz, Germany
* Authors to whom correspondence should be addressed: C.F.: christoph.foerster@uni-mainz.de, K.H.: katja.heinze@uni-mainz.de

General Procedures

All reactions and measurements were performed under argon atmosphere unless otherwise noted. Gloveboxes (UniLab/MBraun − Ar 4.8, O_2 < 1 ppm, H_2O < 0.1 ppm) were used to store and weight sensitive compounds for synthesis as well as to prepare samples that require absence of oxygen and water. The reagents were purchased from commercial suppliers (ABCR, Acros Organics, Alfa Aesar, Fischer Scientific and Sigma Aldrich). Dichloromethane was dried and distilled from CaH_2, 1,4-dioxane from sodium, THF and 2-methyl-tetrahydrofuran from potassium. Deuterated solvents were purchased from euriso-top and Deutero GmbH and were dried by the same procedure as above and stored over molecular sieve (3 Å). The compounds H_2bpep[1] and M[N(SiMe$_3$)$_2$]$_2$[2] were prepared according to literature procedures.

All NMR Spectra were recorded on a Bruker Avance DRX 400 spectrometer at 400.42 MHz (^{1}H), 100.70 MHz (^{13}C{^{1}H}), 149.23 MHz (^{119}Sn) and 83.79 MHz (^{207}Pb). All data were evaluated with the software *MestReNova 12.0.4-22023*. All resonances are reported in ppm versus the solvent signal as internal standard (^{1}H; (^{13}C) NMR: THF-d_8: δ = 1.72, 3.58; (25.31, 67.21) ppm; DMSO-d_6: δ = 2.50; (29.84, 206.26) ppm)[3] or external standards for ^{119}NMR (SnMe$_4$, δ = 0 ppm) and ^{207}Pb (PbMe$_4$, δ = 0 ppm). (s) = singlet, (d) = doublet, (t) = triplet.

Electrospray ionization ESI(+) mass spectra were recorded on an *Agilent 6545 QTOF-MS* spectrometer.

Elemental analyses were performed by the central analytic service of the Department of Chemistry of the University of Mainz using an *Elementar vario EL Cube* or by the Mikroanalytisches Labor Kolbe, c/o Fraunhofer Institut UMSICHT, Oberhausen, Germany.

UV/VIS/NIR spectra were recorded on a *Jasco V-770* spectrometer using gastight 1.00 cm quartz cells with a Schott valve. Measurements in THF were carried out in special UVasol®-THF for spectroscopy from Sigma Aldrich. The extinction coefficients are given at maximum absorption and for shoulders, highlighted as sh.

Steady-state emission spectra and photoluminescent decay curves (solution and solid-state samples) were measured with a *FLS1000 spectrometer* from *Edinburgh Instruments* equipped with a cooled photomultiplier detector PMT-980 and a Lifetime HSPMT-920. A xenon arc lamp Xe2 (450 W) was used for excitation in steady-state measurements. Time-resolved luminescence experiments were conducted using the μs-xenon-flashlamp *μF2* (pulse width ca. 2 μs) and a picosecond pulsed diode laser EPL-375 as excitation source. Measurements at low temperature were carried out using a liquid nitrogen cooled cryostat *Optistat DN* from *Oxford Instruments*. Absolute luminescence quantum yields Φ were determined using the MicrostatN from Oxford Instruments combined with the Cryosphere from Edinburgh Instruments. Relative uncertainty of Φ is estimated to be ±20%. The Arrhenius fits were performed on basis of eq. 1 (Fig. 6b and 7b; Table 2, main text).[4] A global fit of the data of **1^{Sn}** did not give satisfactory results due to the large range of $k(T)$. Therefore, E_{a1}, dominant in the high temperature region, was obtained from a linear Arrhenius fit by including four data points between 293 and 225 K. E_{a1} was kept constant, while the remaining parameters k_0, A_1, E_{a2} and A_2 were optimised, including the eight data points from 77 to 175 K. In case of **1^{Pb}**, a global fit in the range 200 to 77 K gave satisfactory results. An alternative, more sophisticated approach with the assumption of excited states in thermal equilibrium during decay, following a Boltzmann distribution,[5] gave identical fit results within error, indicating that the fit, according to eq. 1 is sufficiently precise.

DFT Calculations

All calculations were performed using the quantum computing suite 5.0.2.[6,7] Geometry optimization was performed using (un-)restricted Kohn-Sham orbitals DFT (UKS/RKS) and the B3LYP functional[8–10] in combination with Ahlrich's split valance triple-zeta basis set def2-TZVPP,[11] old-ZORA-TZVPP (Sn) and SARC-ZORA-TZVPP (Pb) with the auxiliary basis SARC/J.[12–16] Tight convergence criteria were chosen for DFT calculations (keywords *tightscf* and *tightopt*). All DFT calculations make use of the resolution of identity (Split-RI-J) approach for the Coulomb term in combination with the chain-of-spheres approximation for the exchange term (keyword *RIJCOSX*).[17,18] The zeroth order regular approximation was used to describe relativistic effects in all calculations (keyword *ZORA*).[12–16,19,20] To account for solvent effects, a conductor-like screening model (keyword *CPCM*(thf)) modeling thf was used in all calculations.[21,22] Atom-pairwise dispersion correction was performed with the Becke-Johnson damping scheme (keyword *D3BJ*).[23,24] A numerical frequency calculation confirmed that the optimized geometry corresponds to a minimum structure or a transition state structure, respectively. Explicit counter ions and/or solvent molecules were not taken into account, if not explicitly noted. The 2D relaxed potential energy surface scans with 121 points were performed on the CPCM-(THF)-RIJCOSX-UB3LYP-D3BJ-ZORA/def2-SVP/old-ZORA-TZVPP(Sn)/SARC-ZORA-TZVPP(Pb) level with subsequent single-point calculations at higher level (CPCM-(THF)-RIJCOSX-(U)B3LYP-D3BJ-ZORA/def2-TZVPP/old-ZORA-TZVPP(Sn)/SARC-ZORA-TZVPP(Pb)). Transition states were localised, using the *optts* keyword and assigned with a subsequent calculation of the internal reaction coordinate (keyword *IRC*). Fifty vertical spin-allowed transitions were calculated by TD-DFT. The charge transfer number analyses of the TD-DFT calculated transitions were done using TheoDORE 2.4.[25] All calculations were computed on the Elwetritsch supercomputer at the Technical University of Kaiserslautern (elwe.rhrk.uni-kl.de). This is a member of the AHRP (Alliance for High Performance Computing Rhineland-Palatinate).

Crystal Structure Determination

Intensity data for crystal structure determination were collected with a STOE IPDS-2T diffractometer from STOE & CIE GmbH with an Oxford cooling using Mo-Kα radiation (λ = 0.71073 Å). The diffraction frames were integrated using the STOE X-Area[26] software package and were corrected for absorption with STOE X-Red of the X-Area[26] software package. The structures were solved with SHELXT[27] and refined by the full-matrix method based on F^2 using SHELXL[28] of the SHELX[29] software package and the ShelXle[30] graphical interface. All non-hydrogen atoms were refined anisotropically while the positions of all hydrogen atoms were generated with appropriate geometric constraints and allowed to ride on their respective parent atoms with fixed isotropic thermal parameters. Crystallographic data for the structures reported in this paper have been deposited with the Cambridge Crystallographic Data Centre as supplementary publication no. CCDC-2211126 for **1^{Sn}** and no. CCDC-2211125 for **$(1^{Sn})_2$(diox)**.

Crystallographic Data of 1^{Sn}

$C_{15}H_{13}N_3Sn$ (353.97); trigonal; *R*3; *a* = 28.972(4) Å, *b* = 28.972(4) Å, *c* = 8.1427(16) Å; α = 90°; β = 90°; γ = 120°; *V* = 5919(2) Å^3; *Z* = 18; density, calcd. = 1.787 g cm^{-3}, *T* = 120(2) K, μ = 1.931 mm^{-1}; *F*(000) = 3132; crystal size 0.220 × 0.180 × 0.100 mm^3; θ = 2.435 to 27.944 deg.; −37≤h≤38, −37≤k≤38, −10≤l≤10; rfln collected = 38896; rfln unique = 6268 [*R*(int) = 0.0603]; completeness to θ = 25.242 deg.: 100.0%; absorption correction: integration; max. and min. transmission 0.8301 and 0.6389; data 6268; restraints 161, parameters 455; goodness-of-fit on F^2 = 1.133; final indices [$I > 2\sigma(I)$] R_1 = 0.0370, wR_2 = 0.0952; *R* indices (all data) R_1 = 0.0378, wR_2 = 0.0958; largest diff. peak and hole 1.565 and −0.495 e.Å^{-3}.

Crystallographic Data of $(1^{Sn})_2$(diox)

$C_{34}H_{34}N_6O_2Sn_2$ (796.05); monoclinic; *I*2/a; *a* = 15.389(3) Å, *b* = 8.8015(18) Å, *c* = 23.005(9) Å; α = 90°; β = 101.75(3)°; γ = 90°; *V* = 3050.6(15) Å^3; *Z* = 4; density, calcd. = 1.733 g cm^{-3}, *T* = 120(2) K, μ = 1.680 mm^{-1}; *F*(000) = 1584; crystal size 0.800 × 0.343 × 0.040 mm^3; θ = 2.484 to 27.902 deg.; −20≤h≤20, −11≤k≤9, −30≤l≤30; rfln collected = 13572; rfln unique = 3638 [*R*(int) = 0.0177]; completeness to θ = 25.242 deg.: 99.9%; absorption correction: integration; max. and min. transmission 0.9292 and 0.5064; data 3638; restraints 0, parameters 200; goodness-of-fit on F^2 = 1.110; final indices [$I > 2\sigma(I)$] R_1 = 0.0293, wR_2 = 0.0719; *R* indices (all data) R_1 = 0.0309, wR_2 = 0.0730; largest diff. peak and hole 2.919 and −0.787 e.Å^{-3}.

Synthesis of Sn(bpep) 1^{Sn}

$Sn[(N(SiMe_3)_2]_2$ (556 mg,1.27 mmol, 1.01 eq) in dichloromethane (5 mL) was added to a stirred solution of H_2bpep (300 mg, 1.26 mmol, 1.00 eq) in dichloromethane (5 mL). After stirring for 15 h at ambient temperature, the precipitate was separated from the solution and washed with dichloromethane (3 × 3 mL) and dried under reduced pressure. $\mathbf{1^{Sn}}$ (330 mg, 74%) was obtained as a colourless solid.

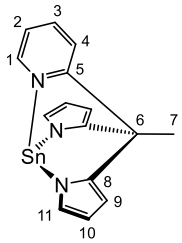

^{1}H NMR (THF-d_8): δ = 8.38−8.36 (m, 1H, H^1), 7.68 (ddd, $^3J_{HH}$ = 8.1, 7.4, $^4J_{HH}$ = 1.8 Hz, 1H, H^3), 7.60 (dt, $^3J_{HH}$ = 8.1, $^4J_{HH}$ = 1.2 Hz, 1H, H^4), 7.06 (ddd, $^3J_{HH}$ = 7.4, 5.2, $^4J_{HH}$ = 1.2 Hz, 1H, H^2), 6.77 (dd, $^3J_{HH}$ = 2.3, $^4J_{HH}$ = 1.4 Hz, 2H, H^{11}), 6.01 (dd, $^3J_{HH}$= 3.1, $^4J_{HH}$ = 1.4 Hz , 2H, H^9), 5.84 (dd, $^3J_{HH}$= 3.1, 2.4 Hz , 2H, H^{10}), 2.28 (s, 3H, H^7) ppm.
^{13}C NMR (THF-d_8): δ = 165.9 (s, C^5), 147.7 (s, C^1), 141.6 (s, C^3), 139.0 (s, C^8), 124.0 (s, C^{11}), 122.4 (s, C^2), 120.2 (s, C^4), 107.2 (s, C^{10}), 103.2 (s, C^9), 46.9 (s, C^6), 20.9 (s, C^7) ppm.
^{119}Sn NMR (THF-d_8): δ = −401.2 ppm.
MS (ESI$^+$; CH_3CN): *m/z* (%) = 378.00 (7) [$\mathbf{1^{Sn}}$+Na^+], 393.98 (64) [$\mathbf{1^{Sn}}$+K^+], 731.02 (20) [2 $\mathbf{1^{Sn}}$+Na^+], 746.99 (100) [2 $\mathbf{1^{Sn}}$+K^+].
Elemental analysis calcd. for $C_{15}H_{13}N_3Sn$: C, 50.89; H, 3.70; N, 11.87. Found: C, 50.50; H, 3.67; N, 11.74.
UV/Vis (THF): λ_{max} (ε) = 340 (534, sh), 258 (4070), 236 (4380) nm (M^{-1} cm^{-1}).

Synthesis of Pb(bpep) 1^{Pb}

$Pb[(N(SiMe_3)_2]_2$ (1120 mg,2.13 mmol, 1.01 eq) in dichloromethane (8 mL) was added to a stirred solution of H_2bpep (500 mg, 2.11 mmol, 1.00 eq) in dichloromethane (8 mL). A colourless precipitate was formed immediately. After stirring for 15 h at ambient temperature, the precipitate was separated from the solution and washed with dichloromethane (3 × 5 mL) and dried under reduced pressure. $\mathbf{1^{Pb}}$ (556 mg, 63%) was obtained as a colourless solid.

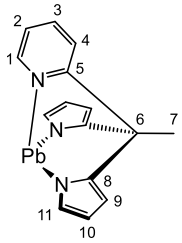

^{1}H NMR (DMSO-d_6): δ = 8.57 (dd, $^3J_{HH}$ = 5.2, $^4J_{HH}$ = 1.7 Hz , 1H, H^1), 7.83 (td, $^3J_{HH}$ = 8.0, $^4J_{HH}$ = 1.7 Hz, 1H, H^3), 7.76 (dt, $^3J_{HH}$ = 8.0, $^4J_{HH}$ = 1.5 Hz, 1H, H^4), 7.30 (ddd, $^3J_{HH}$ = 8.0, 5.2, $^4J_{HH}$ = 1.5 Hz, 1H, H^2), 6.86-6.83 (m, 2H, H^{11}), 6.17 (dd, $^3J_{HH}$= 3.0, $^4J_{HH}$ = 1.5 Hz , 2H, H^9), 5.96 (dd, $^3J_{HH}$= 3.0, 2.2 Hz 2H, H^{10}), 2.27 (s, 3H, H^7) ppm.
^{13}C NMR (DMSO-d_6): δ = 165.0 (s, C^5), 147.6 (s, C^1), 140.1 (s, C^8), 139.8 (s, C^3), 124.0 (s, C^{11}), 121.3 (s, C^2), 119.2 (s, C^4), 105.9 (s, C^{10}), 102.3 (s, C^9), 50.2 (s, C^6), 22.0 (s, C^7) ppm.
^{207}Pb NMR (DMSO-d_6): δ = 388.3 ppm.
MS (ESI$^+$; DMSO/CH_3CN): *m/z* (%) = 482.05 (19) [$\mathbf{1^{Pb}}$+K^+], 893.19 (10) [2 $\mathbf{1^{Pb}}$+Li^+], 909.16 (20) [2 $\mathbf{1^{Pb}}$+Na^+], 925.14 (25) [2 $\mathbf{1^{Pb}}$+K^+].
Elemental analysis calcd. for $C_{15}H_{13}N_3Pb$: C, 40.72; H, 2.96; N, 9.50. Found: C, 40.15; H, 3.02; N, 9.29.
UV/Vis (DMSO): λ_{max} (ε) = 312 (1540, sh), 278 (3010), 264 (5660) nm (M^{-1} cm^{-1}).

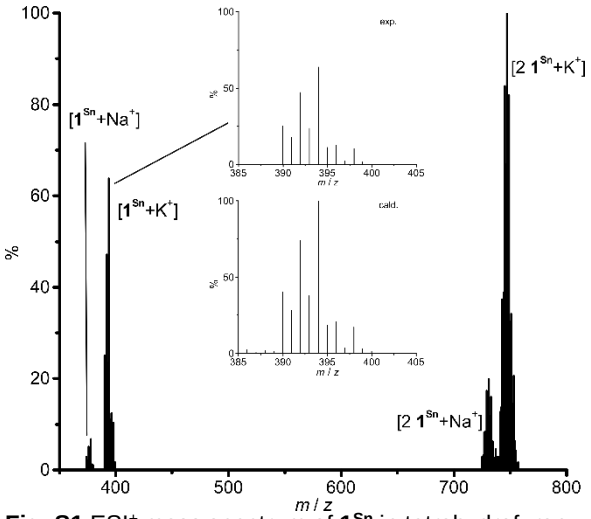

Fig. S1 ESI$^+$ mass spectrum of $\mathbf{1}^{Sn}$ in tetrahydrofuran with insets of the experimentally found and calculated isotope pattern for [$\mathbf{1}^{Sn}$+K$^+$].

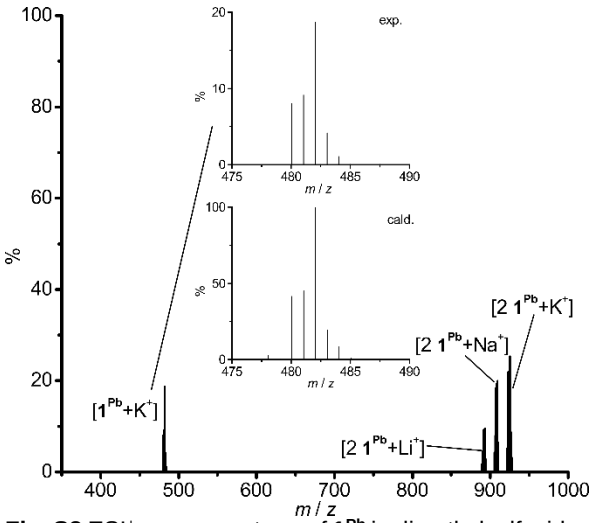

Fig. S2 ESI$^+$ mass spectrum of $\mathbf{1}^{Pb}$ in dimethylsulfoxide with insets of the experimentally found and calculated isotope pattern for [$\mathbf{1}^{Pb}$+K$^+$].

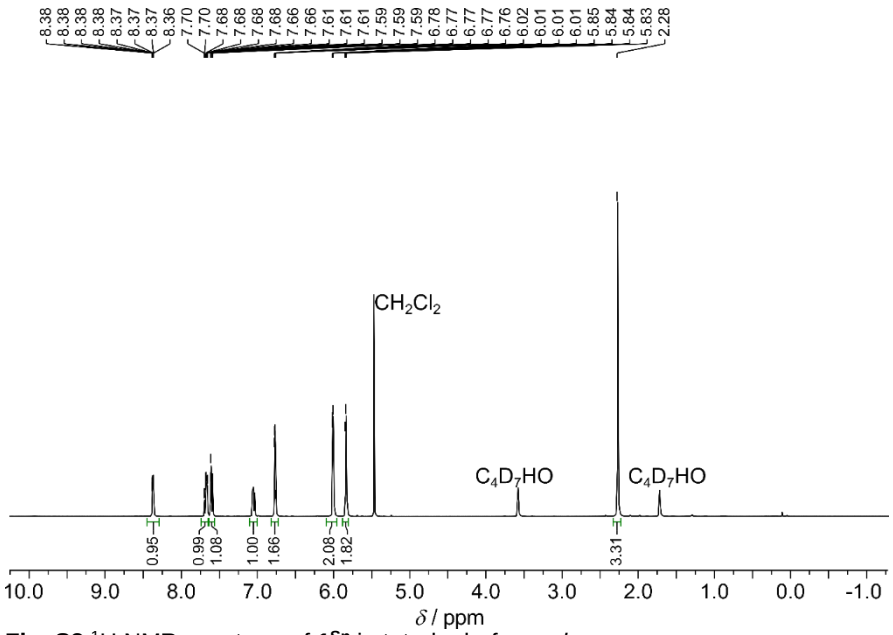

Fig. S3 ^{1}H NMR spectrum of **1^{Sn}** in tetrahydrofuran-d_8.

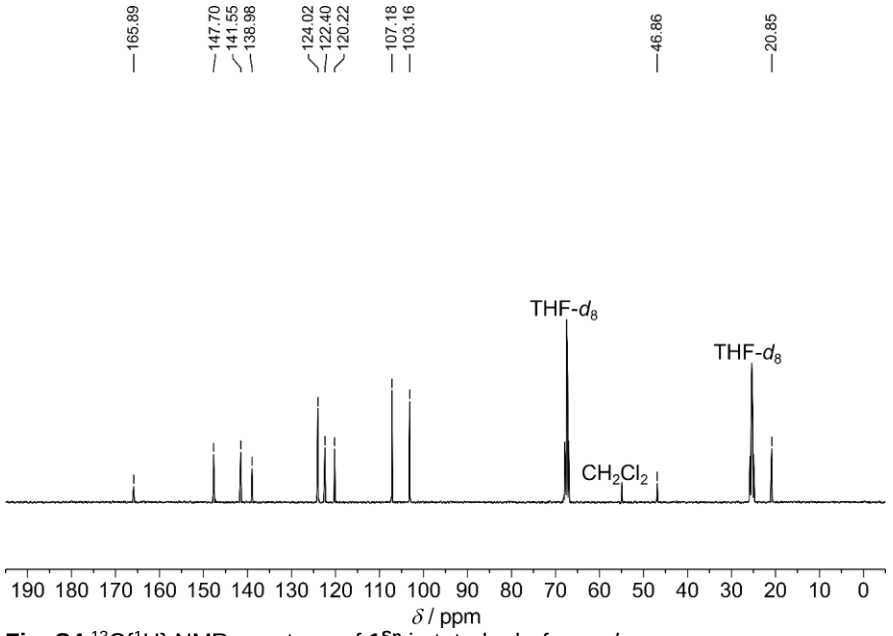

Fig. S4 ^{13}C{^{1}H} NMR spectrum of **1^{Sn}** in tetrahydrofuran-d_8.

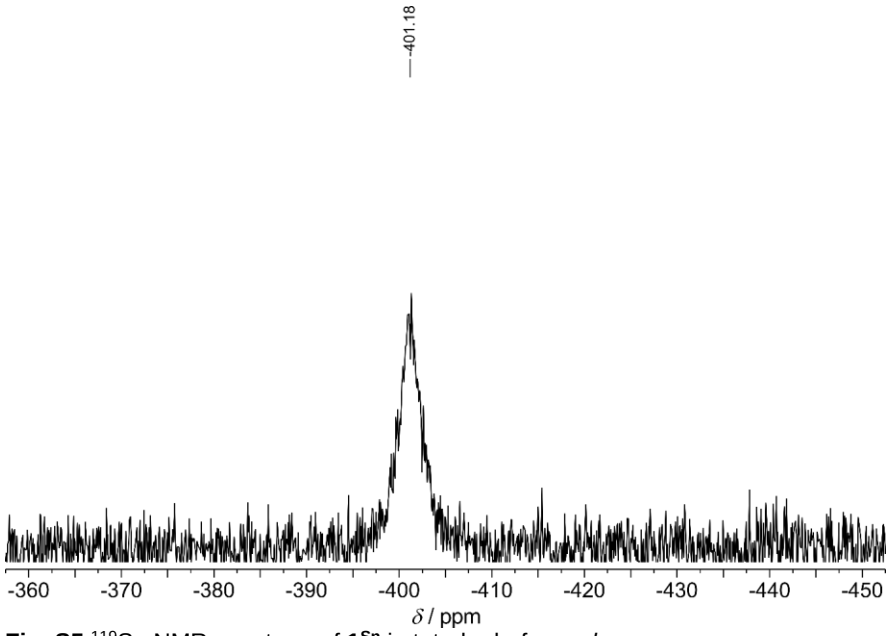

Fig. S5 ^{119}Sn NMR spectrum of **1^{Sn}** in tetrahydrofuran-d_8.

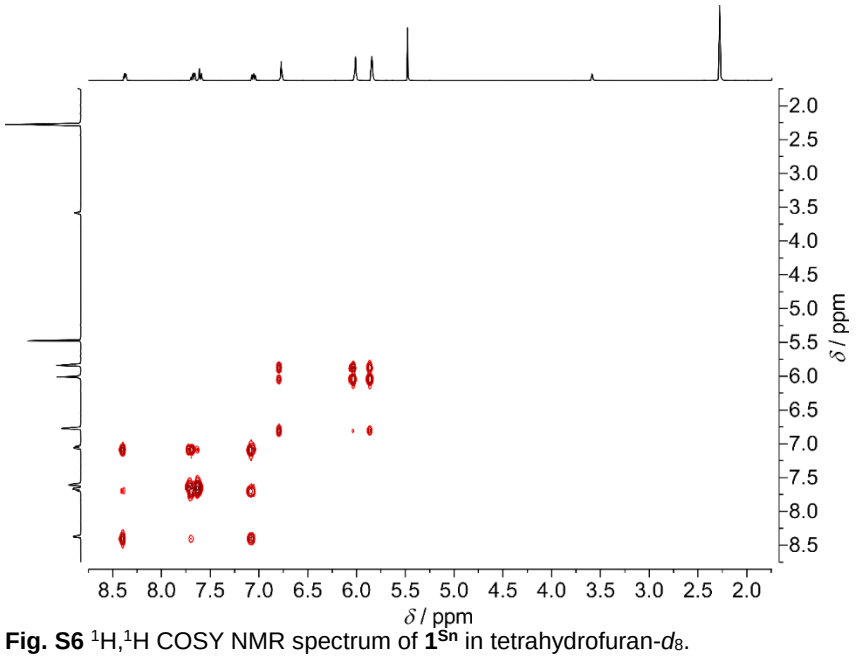

Fig. S6 ^{1}H,^{1}H COSY NMR spectrum of **1^{Sn}** in tetrahydrofuran-d_8.

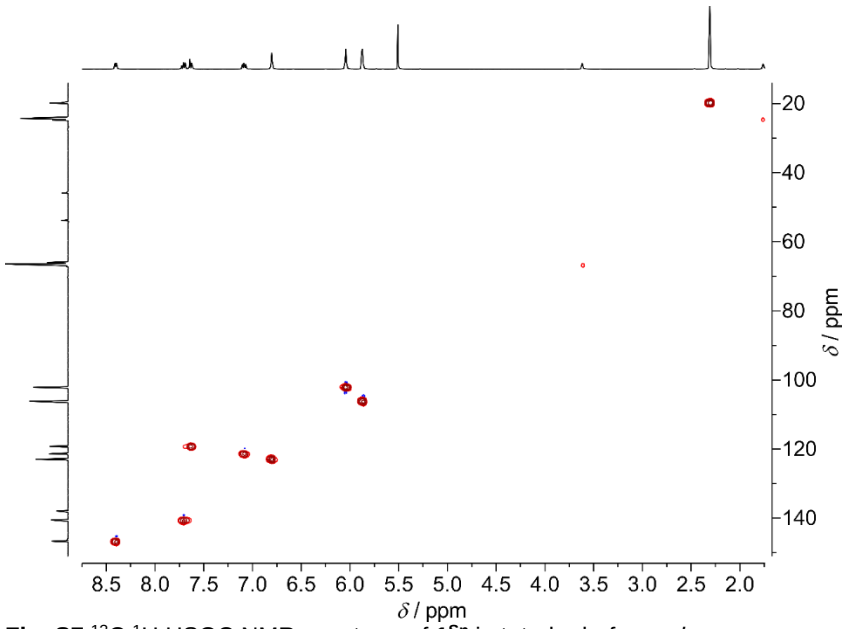

Fig. S7 $^{13}C,^{1}H$ HSQC NMR spectrum of **1^{Sn}** in tetrahydrofuran-d_8.

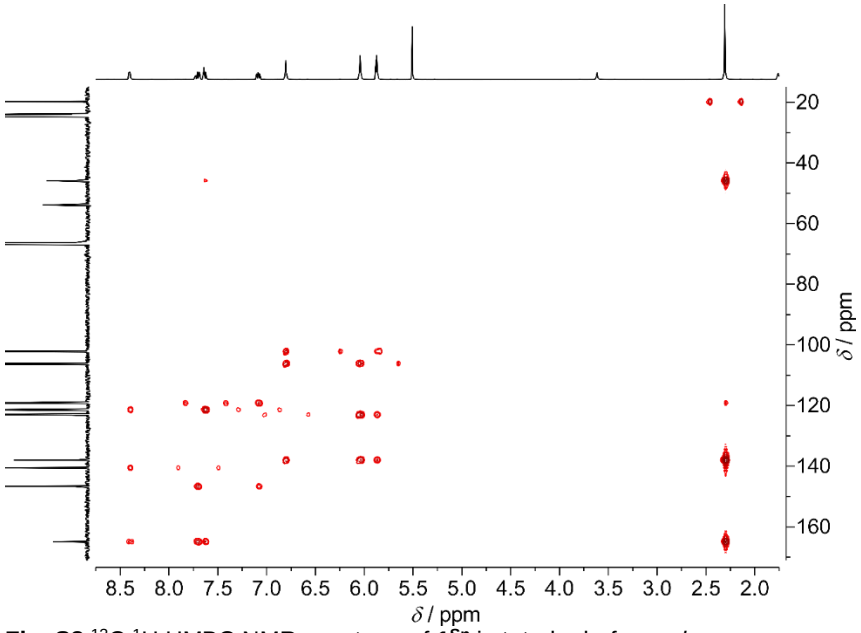

Fig. S8 $^{13}C,^{1}H$ HMBC NMR spectrum of **1^{Sn}** in tetrahydrofuran-d_8.

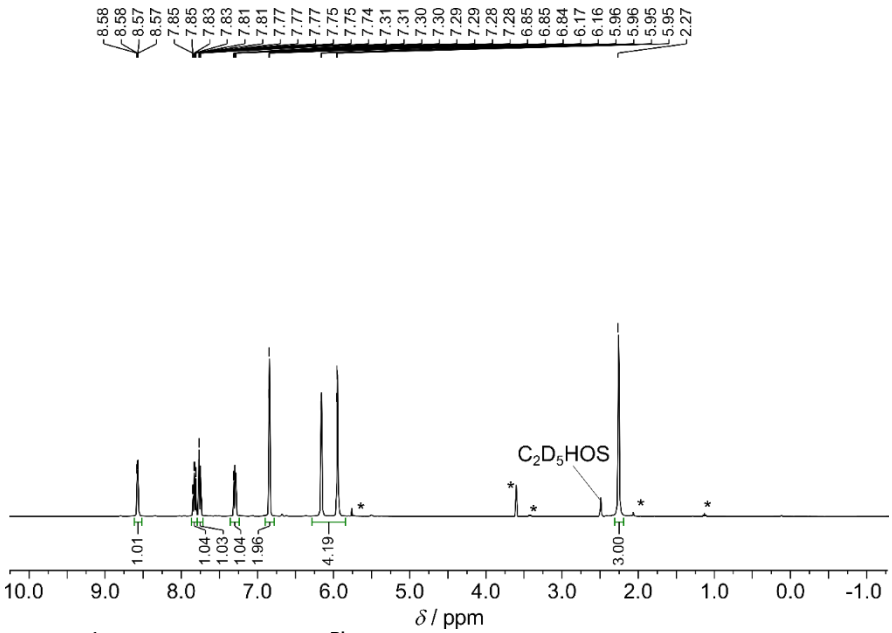

Fig. S9 ^{1}H NMR spectrum of **1^{Pb}** in dimethylsulfoxide-d_6. The asterisks denote solvent impurities.

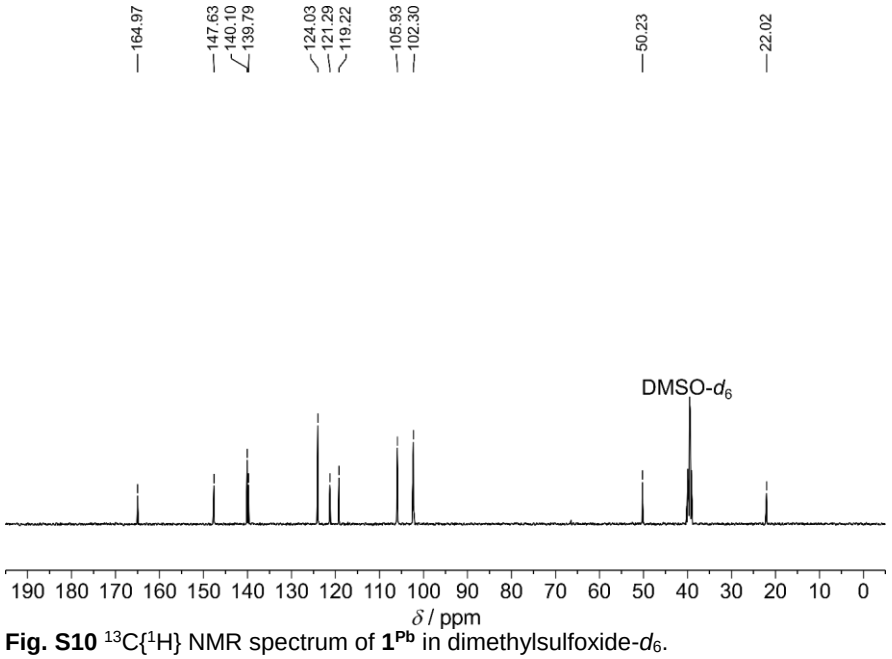

Fig. S10 ^{13}C{^{1}H} NMR spectrum of **1^{Pb}** in dimethylsulfoxide-d_6.

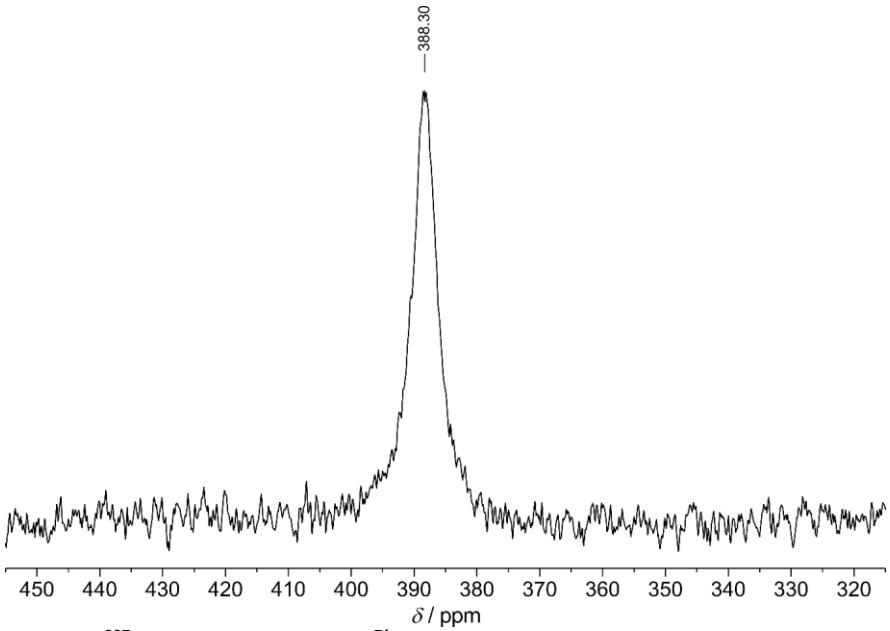

Fig. S11 ^{207}Pb NMR spectrum of **1^{Pb}** in dimethylsulfoxide-d_6.

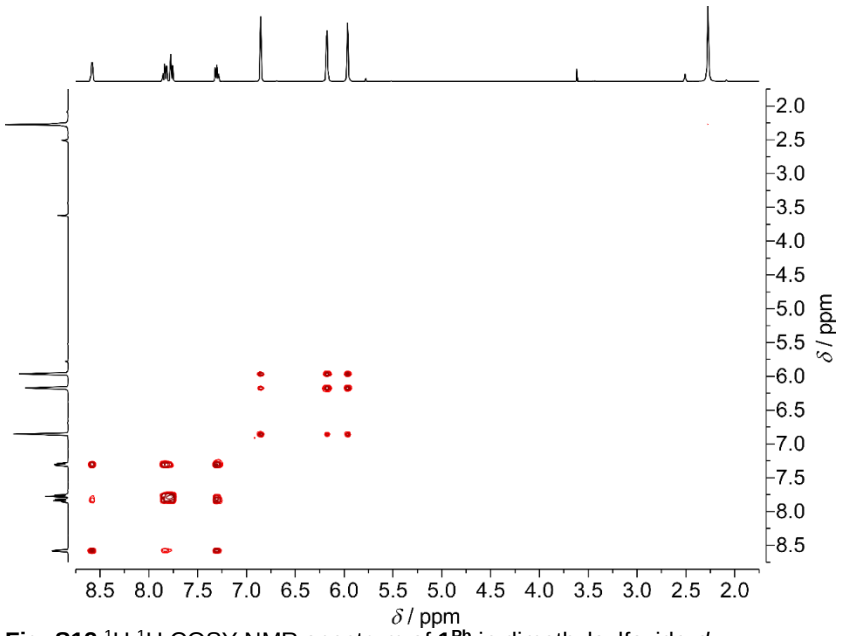

Fig. S12 ^{1}H,^{1}H COSY NMR spectrum of **1^{Pb}** in dimethylsulfoxide-d_6.

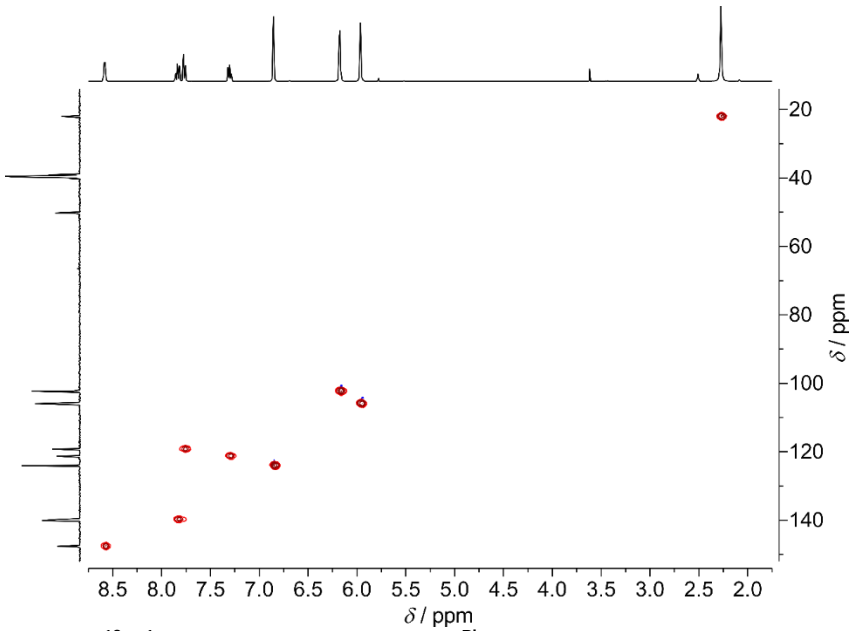

Fig. S13 $^{13}C,^{1}H$ HSQC NMR spectrum of $\mathbf{1}^{Pb}$ in dimethylsulfoxide-d_6.

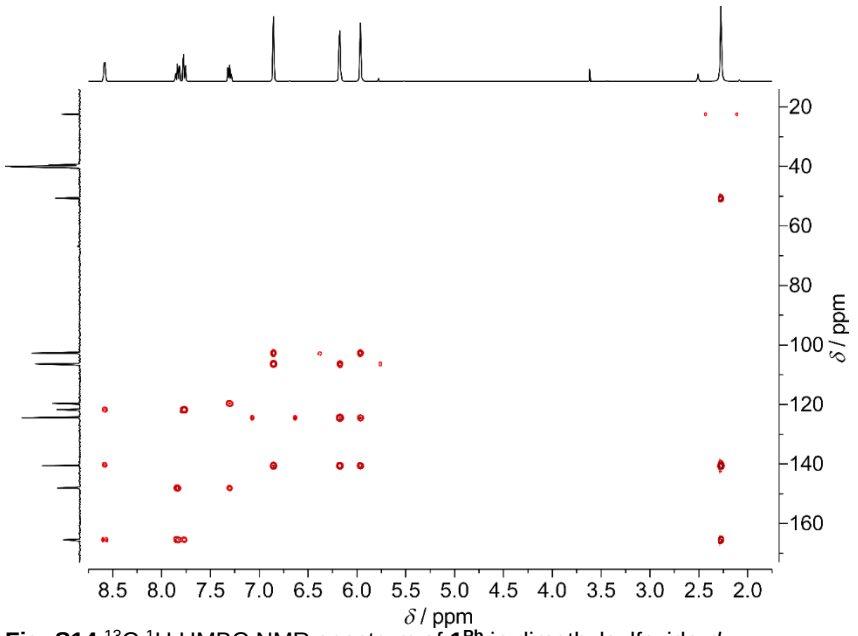

Fig. S14 $^{13}C,^{1}H$ HMBC NMR spectrum of $\mathbf{1}^{Pb}$ in dimethylsulfoxide-d_6.

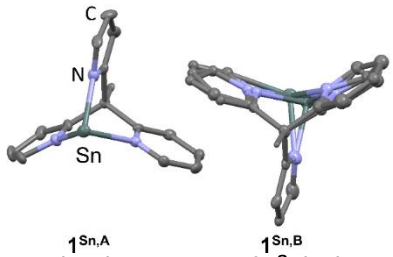

Fig. S15 Molecular structure of $\mathbf{1}^{Sn}$ in the solid state (trigonal space group R_3) with two molecules $\mathbf{1}^{Sn,A}$ and disordered $\mathbf{1}^{Sn,B}$ in the asymmetric unit. H atoms omitted, thermal ellipsoids at 50% probability level.

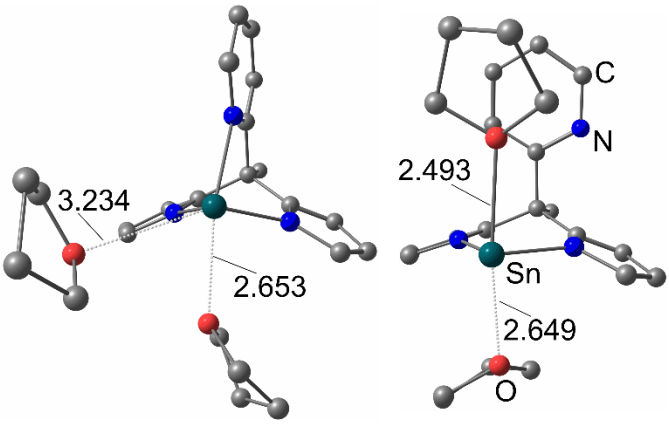

***cis*-1^{Sn}(thf)$_2$** **0** ***trans*-1^{Sn}(thf)$_2$** **+10**

Fig. S16 DFT optimised geometries of ***cis-/trans*-1^{Sn}(thf)$_2$** with relative Gibbs free energies ΔG_{298} at 298 K in kJ mol^{-1} and distances in Å.

Table S1 Selected structural parameters in Å and deg. of solid state structures of **1^{Sn}** (molecule A, **1^{Sn,A}**) and **(1^{Sn})$_2$(diox)** from XRD analyses and of DFT calculated geometry optimised structures of **1^{Sn}** and **1^{Sn}(thf)** in the ^{1}GS and ^{3}ILCT/^{3}LMCT/^{3}MLCT states.

	1^{Sn,A} (XRD)	**(1^{Sn})$_2$(diox)** (XRD)	^{1}**1^{Sn}** (DFT)	^{3ILCT}**1^{Sn}** (DFT)	^{3LMCTpy}**1^{Sn}** (DFT)	^{3LMCTpyr}**1^{Sn}** (DFT)
Sn–N^{py}	2.317(5)	2.375(2)	2.341	2.147	3.897	2.323
Sn–N^{pyr}	2.130(5) 2.149(7)	2.125(2) 2.152(2)	2.146 2.147	2.218 2.220	2.248 2.240	3.726 2.176
Sn–O		2.547(2)				
N^{pyr}–Sn–N^{pyr}	84.1(2)	84.08(9)	85.1	79.4	79.3	81.5
N^{py}–Sn–N^{pyr}	80.24(18) 79.0(2)	77.93(8) 79.93(8)	80.3 80.3	83.2 83.3	54.9 80.1	81.3 56.5
O–Sn–N^{py}		155.98(7)				
O–Sn–N^{pyr}		80.94(8) 87.07(8)				
Sn–N^{py}–C^{py}–C^{backbone}	2.1	2.4	0.3	0.1	83.0	5.1
Sn–N^{pyr}–C^{pyr}–C^{backbone}	5.5	3.7	0.2	5.1	13.7	78.6

	^{1}**1^{Sn}(thf)** (DFT)	^{3ILCT}**1^{Sn}(thf)** (DFT)	^{3LMCTpy}**1^{Sn}(thf)** (DFT)	^{3LMCTpyr}**1^{Sn}(thf)** (DFT)	^{3MLCT}**1^{Sn}(thf)** (DFT)
Sn–N^{py}	2.441	2.182	3.917	2.451	2.127
Sn–N^{pyr}	2.155 2.159	2.221 2.225	2.245 2.242	2.202 3.800	2.087 2.083
Sn–O	2.606	2.925	4.378	2.726	2.338
N^{pyr}–Sn–N^{pyr}	85.6	80.6	79.3	80.4	88.4
N^{py}–Sn–N^{pyr}	77.2 77.6	81.6 81.5	54.7 79.9	55.9 77.8	88.9 89.1
O–Sn–N^{py}	149.7	148.6	121.5	158.2	177.5
O–Sn–N^{pyr}	81.6 79.4	76.1 73.3	74.7 62.2	81.5 113.8	90.9 88.4
Sn–N^{py}–C^{py}–C^{backbone}	0.5	0.7	83.2	1.5	0.2
Sn–N^{pyr}–C^{pyr}–C^{backbone}	5.4	8.7	14.4	82.2	3.7
N^{py}–Sn–O	149.7	148.6	121.5	158.2	177.5

Table S2 Selected structural parameters in Å and deg. of DFT calculated geometry optimised structures of **1^{Pb}** and **1^{Pb}(thf)** in the in the ^{1}GS and ^{3}ILCT/^{3}LMCT states.

	^{1}**1**^{Pb} (DFT)	^{3ILCT}**1**^{Pb} (DFT)	^{3LMCTpy}**1**^{Pb} (DFT)	^{3LMCTpyr}**1**^{Pb} (DFT)	^{1}**1**^{Pb}**(thf)** (DFT)	^{3ILCT}**1**^{Pb}**(thf)** (DFT)
Pb−N^{py}	2.455	2.256	3.908	2.459	2.577	2.301
Pb−N^{pyr}	2.260 2.260	2.344 2.344	2.378 2.373	3.703 2.303	2.276 2.270	2.352 2.351
Pb−O					2.700	2.912
N^{pyr}−Pb−N^{pyr}	82.4	76.9	76.8	80.1	83.5	78.2
N^{py}−Pb−N^{pyr}	77.9 77.9	80.5 80.5	54.3 78.4	78.1 55.9	74.6 74.5	78.7 78.5
O−Pb−N^{py}					146.4	146.0
O−Pb−N^{pyr}					81.4 79.7	76.4 74.1
Pb–N^{py}–C^{py}–C^{backbone}	0.2	0.9	85.2	5.0	0.7	1.5
Pb–N^{pyr}–C^{pyr}–C^{backbone}	1.2	5.2	14.8	80.5	3.6	11.1

a)

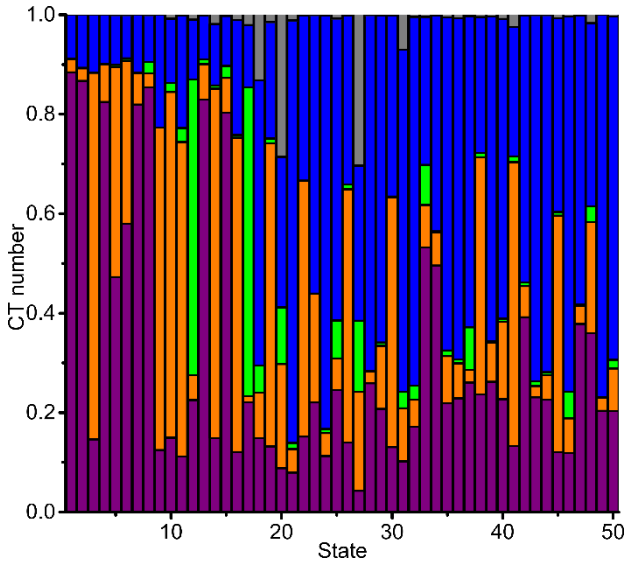

b)

1: 412 nm / 0.01292	2: 382 nm / 0.01257	3: 342 nm / 0.00132	4: 334 nm / 0.03349	5: 319 nm / 0.00275
6: 316 nm / 0.02323	7: 315 nm / 0.01820	8: 303 nm / 0.00988	9: 288 nm / 0.00426	10: 275 nm / 0.05322
11: 272 nm / 0.00111	12: 271 nm / 0.01099	13: 270 nm / 0.00447	14: 262 nm / 0.03356	15: 259 nm / 0.00050
16: 240 nm / 0.00364	17: 234 nm / 0.01379	18: 232 nm / 0.03439	19: 230 nm / 0.01920	20: 225 nm / 0.43686

Fig. S17 a) Charge transfer analysis of the 50 lowest spin-allowed transitions of **1**^{Sn} (purple: ILCT, orange: LMCT, green: MLCT; blue: LC, grey: MC) and b) difference electron densities of the 20 lowest spin-allowed transitions of **1**^{Sn} with the respective wavelength and oscillator strength (purple = electron loss; orange = electron gain) displayed at an isosurface value of 0.005 a.u..

a)

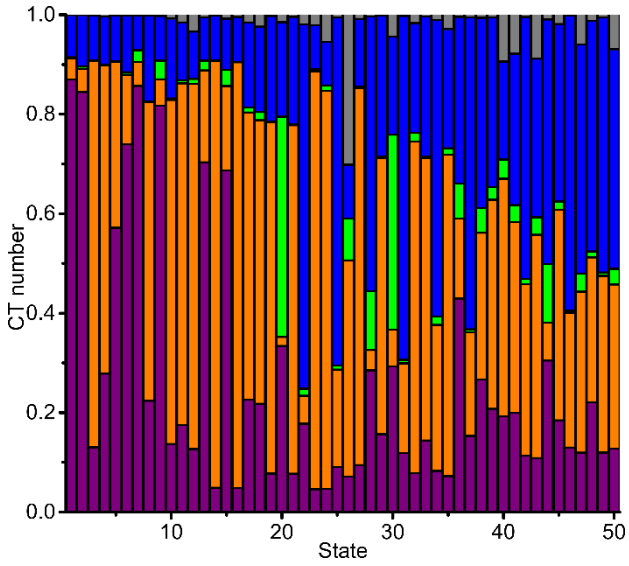

b)

1: 409 nm / 0.01388	2: 382 nm / 0.01230	3: 367 nm / 0.00085	4: 342 nm / 0.00670	5: 338 nm / 0.02678
6: 321 nm / 0.014879	7: 318 nm / 0.01733	8: 310 nm / 0.00951	9: 305 nm / 0.00541	10: 293 nm / 0.00134
11: 292 nm / 0.05506	12: 280 nm / 0.02542	13: 275 nm / 0.01026	14: 273 nm / 0.00001*	15: 265 nm / 0.00115
16: 259 nm / 0.00138*	17: 256 nm / 0.00303	18: 246 nm / 0.016127	19: 243 nm / 0.00146	20: 237 nm / 0.00403

Fig. S18 a) Charge transfer analysis of the 50 lowest spin-allowed transitions of **1**^{Pb} (purple: ILCT, orange: LMCT, green: MLCT; blue: LC, grey: MC) and b) difference electron densities of the 20 lowest spin-allowed transitions of **1**^{Pb} with the respective wavelength and oscillator strength (purple = electron loss; orange = electron gain) displayed at an isosurface value of 0.005 a.u. and 0.0017 a.u. highlighted with an asterisk.

HOMO−5 / −7.6520	HOMO−4 / −7.0270	HOMO−3 / −6.4278	HOMO−2 / −6.2177	HOMO−1 / −5.6078	HOMO / −5.3316
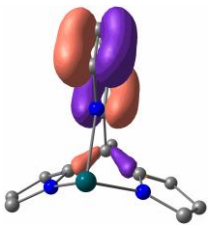	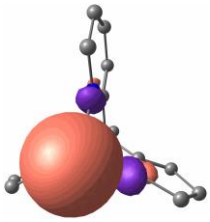	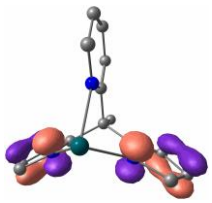	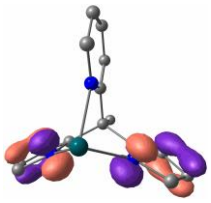	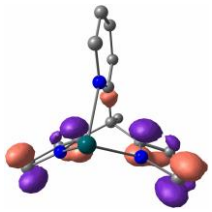	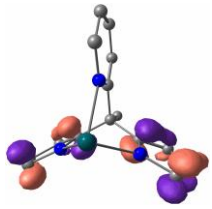
LUMO / −1.6815	LUMO+1 / −0.9956	LUMO+2 / −0.9773	LUMO+3 / −0.2726	LUMO+4 / 0.9456	LUMO+5 / 1.2967
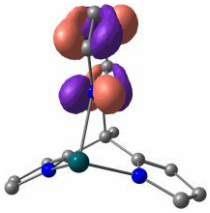	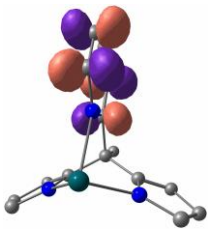	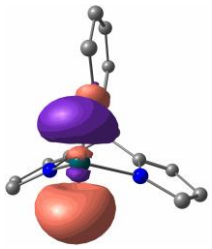	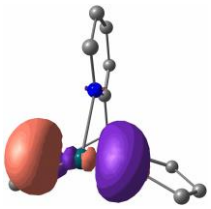	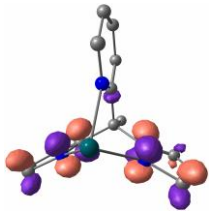	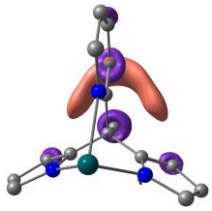

Fig. S19 Selected molecular orbitals of $\mathbf{1}^{Sn}$ with energies given in eV, displayed at an isosurface value of 0.06 a.u..

HOMO−5 / −7.5431	HOMO−4 / −7.5281	HOMO−3 / −6.2457	HOMO−2 / −6.0610	HOMO−1 / −5.4561	HOMO / −5.1999
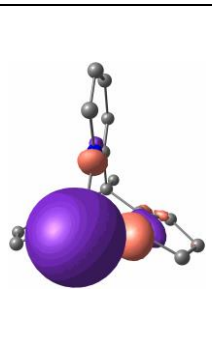	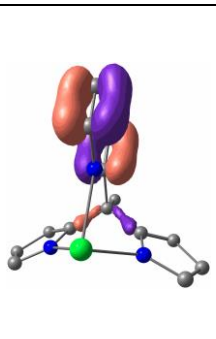	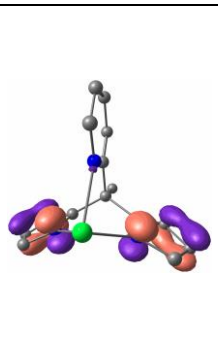	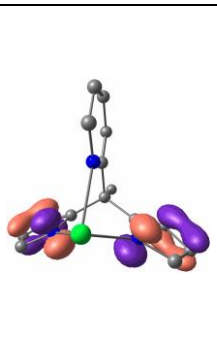	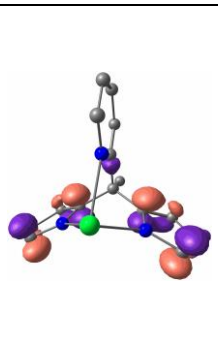	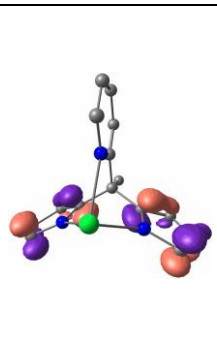
LUMO / −1.5303	LUMO+1 / −1.1150	LUMO+2 / −0.9180	LUMO+3 / −0.4733	LUMO+4 / −0.1050	LUMO+5 / −0.1050
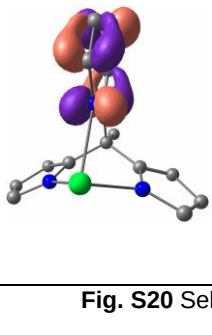	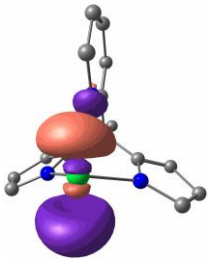	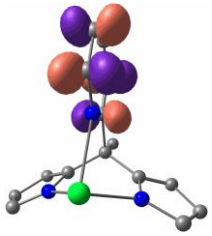	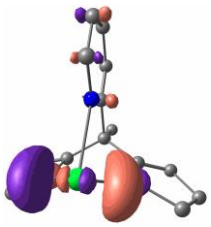	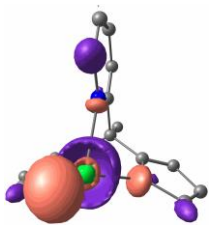	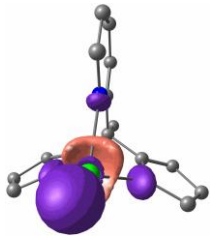

Fig. S20 Selected molecular orbitals of $\mathbf{1}^{Pb}$ with energies given in eV, displayed at an isosurface value of 0.06 a.u..

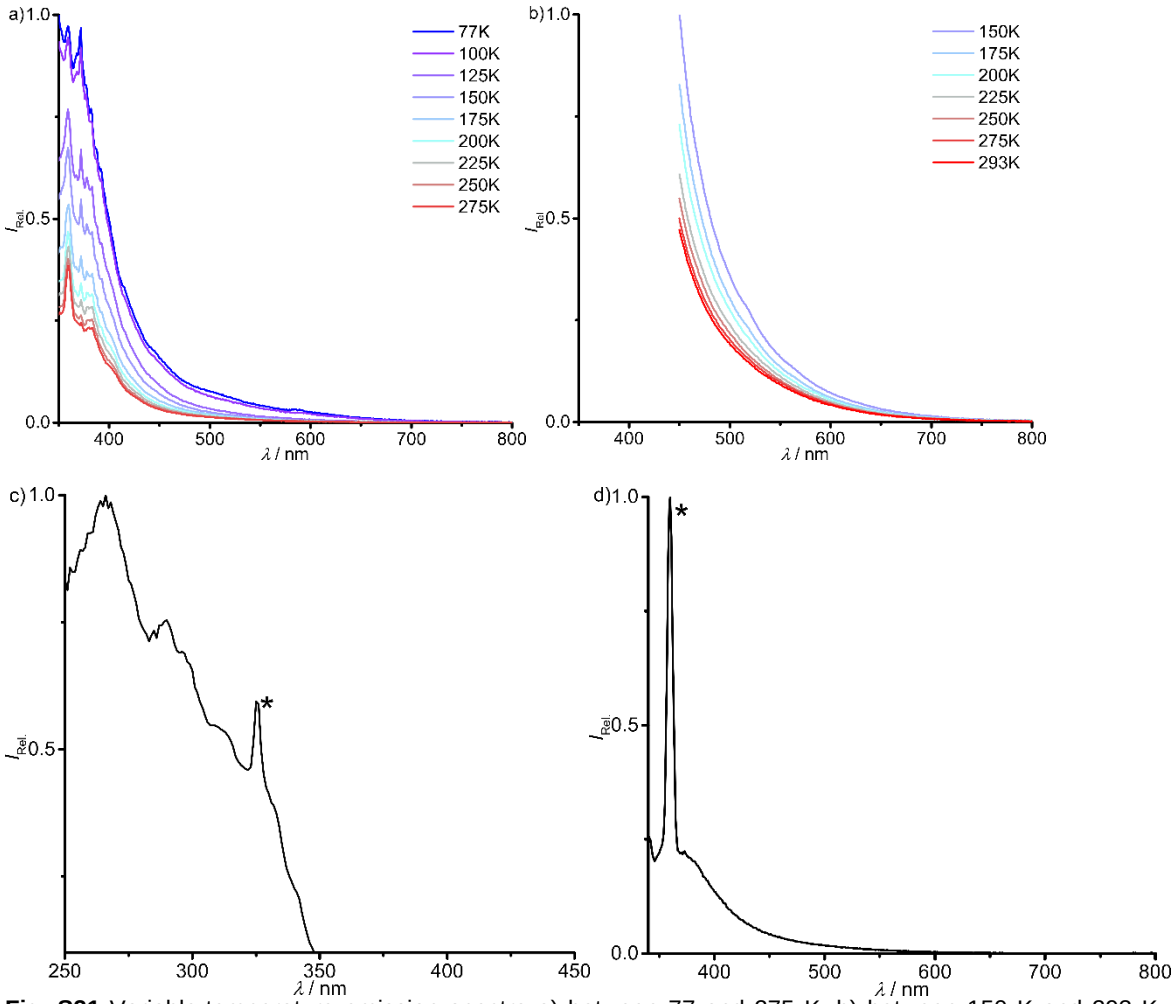

Fig. S21 Variable-temperature emission spectra a) between 77 and 275 K, b) between 150 K and 293 K, c) excitation spectrum (λ_{em} = 380 nm) at 77 K of the unidentified luminescent impurity in 2-methyl-tetrahydrofuran with λ_{exc} = 325 nm and d) emission spectrum of the unidentified impurity in tetrahydrofuran with λ_{exc} = 325 nm at 293 K in the absence of **1^{E}**. The asterisks denote Raman bands of the solvent.

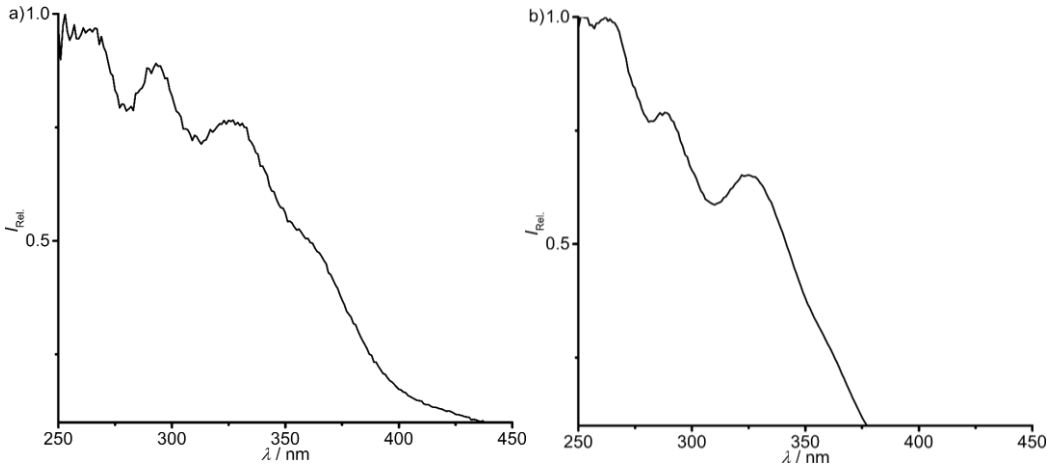

Fig. S22 Excitation spectra of **1^{Sn}** in 2-methyl-tetrahydrofuran at a) 293 (λ_{em} = 580 nm) and b) 77 K (λ_{em} = 530 nm). The high absorbance of the sample at λ < ≈325 nm causes filter effects, yielding distorted excitation spectra.

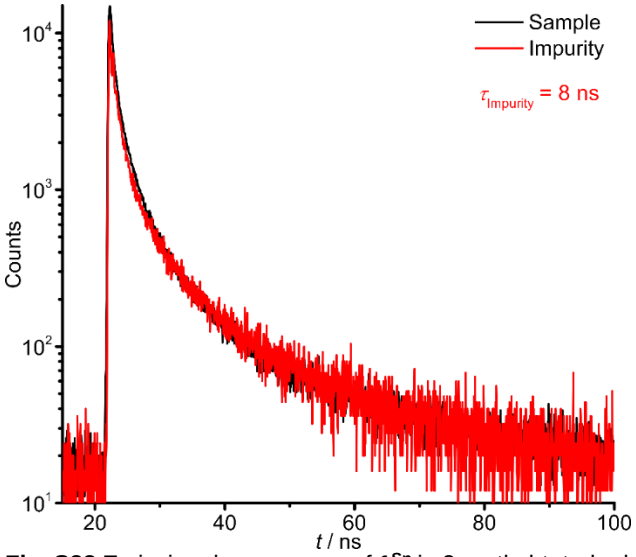

Fig. S23 Emission decay curves of **1^{Sn}** in 2-methyl-tetrahydrofuran after excitation at λ_{exc} = 375 nm with λ_{em} = 575 nm (black curve) and of the unidentified luminescent impurity in 2-methyl-tetrahydrofuran at λ_{exc} = 375 nm with λ_{em} = 400 nm at 150 K (red curve) with luminescence lifetime from monoexponential fit.

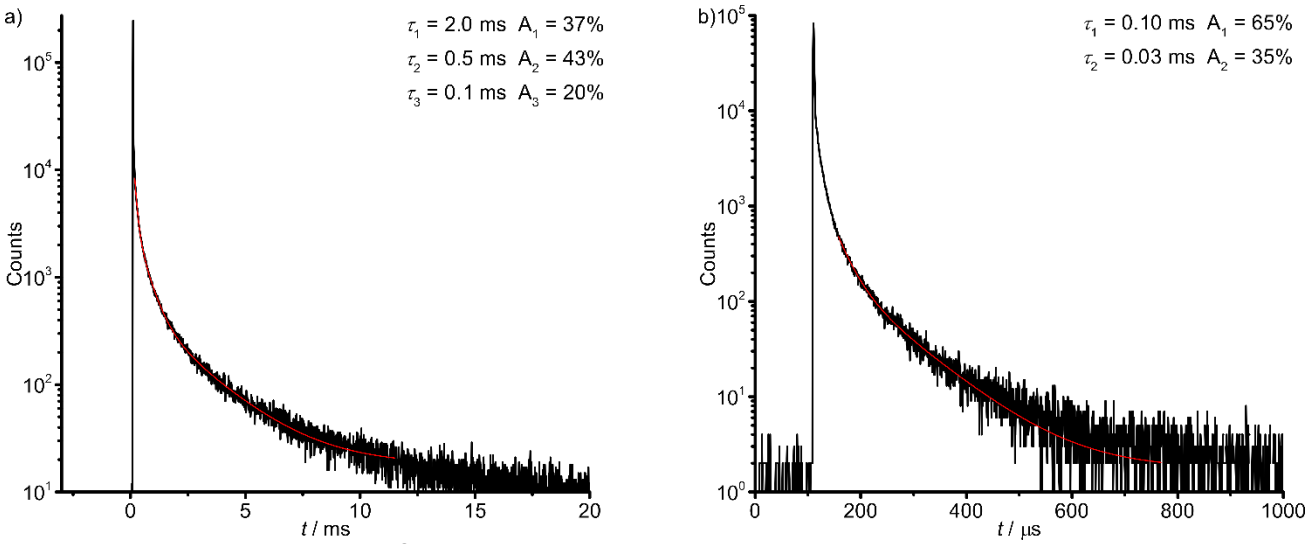

Fig. S24 Emission decay curves of **1^{Sn}** in 2-methyl-tetrahydrofuran at λ_{exc} = 325 nm with λ_{em} = 530 nm and a) 77 K and b) 100 K (black curves), respectively, with luminescence lifetimes with relative emission amplitudes, from tri and biexponential fits (red curves), respectively.

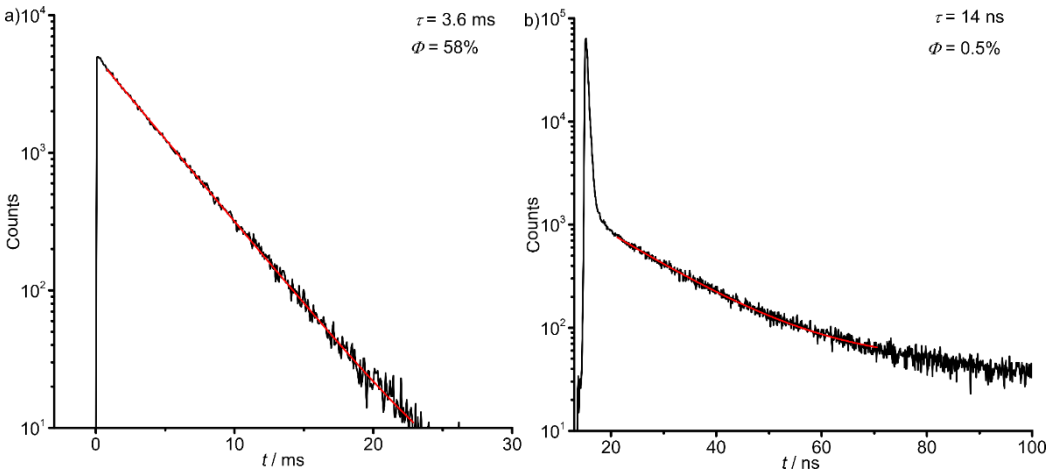

Fig. S25 Emission decay curves of **1^{Sn}** at a) λ_{exc} = 350 nm with λ_{em} = 505 nm and b) at λ_{exc} = 375 nm with λ_{em} = 505 nm at 77 K and 293 K (black curves) in the solid state, respectively, with luminescence lifetimes from monoexponential fits (red curves) and luminescence quantum yields.

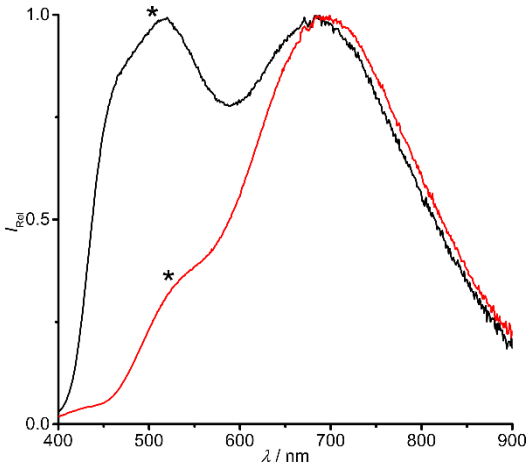

Fig. S26 Normalised emission spectra of a solid sample of **1^{Pb}** with an unidentified minor impurity (oxidation or solvolysis product of **1^{Pb}**), denoted with an asterisk, before (red curve) and after contact to air (black curve) at 77 K with λ_{exc} = 375 nm.

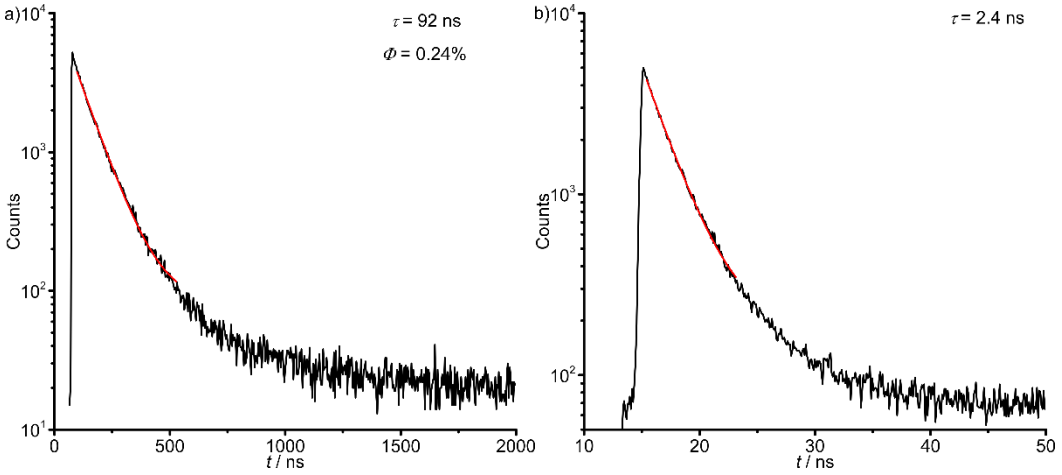

Fig. S27 Emission decay curves of **1^{Pb}** at λ_{exc} = 375 nm with λ_{em} = 700 nm at a) 77 K and b) 200 (black curves), respectively, with luminescence lifetimes from monoexponential fits (red curves) and luminescence quantum yield at 77 K.

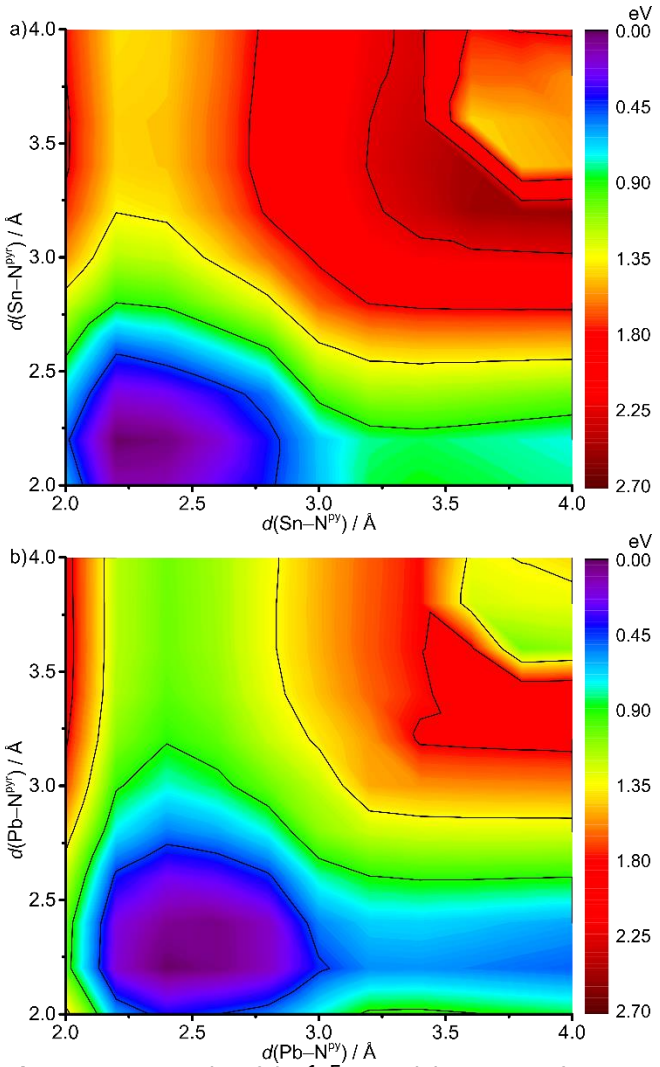

Fig. S28 Contour plot of the $^{1}\mathbf{1}^{E}$ potential energy surfaces, according to single-point energies of a 2D relaxed potential energy surface scan as projection along the E–N^{py} and E–N^{pyr} stretching modes on the triplet hypersurface $^{3}\mathbf{1}^{E}$ of a) $\mathbf{1}^{Sn}$ and b) $\mathbf{1}^{Pb}$ (CPCM-(THF)-RIJCOSX-B3LYP-D3BJ-ZORA/def2-TZVPP/old-ZORA-TZVPP(Sn)/SARC-ZORA-TZVPP(Pb)).

Table S3 Relative Gibbs free energies ΔG_{298} at 298 K of triplet states, ^{1}GS and transition states (TS) in eV, calculated by DFT for $\mathbf{1}^{Sn}$ and $\mathbf{1}^{Pb}$.

	$\mathbf{1}^{Sn}$	$\mathbf{1}^{Pb}$
^{3}**ILCT**	0	0
^{3}**LMCT$_{py}$**	−0.16	−0.38
^{3}**LMCT$_{pyr}$**	+0.10	−0.11
^{1}**GS**	−2.31	−2.33
TS(^{3}ILCT→^{3}LMCT$_{py}$)	+0.25	+0.06
TS(^{3}ILCT→^{3}LMCT$_{pyr}$)	+0.36	–
TS(^{3}LMCT$_{py}$→^{3}LMCT$_{pyr}$)	–	+0.48

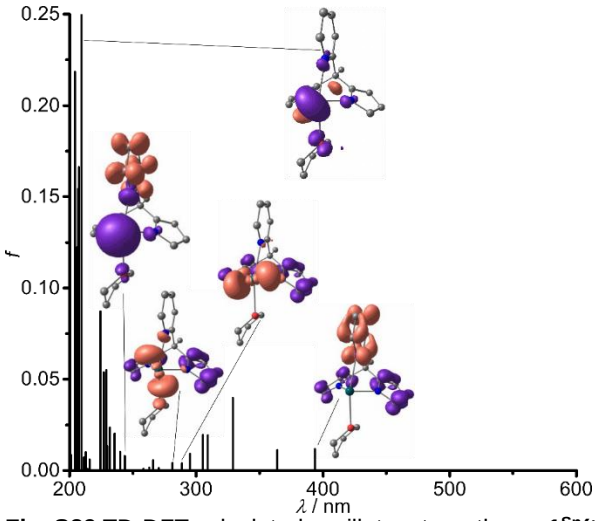

Fig. S29 TD-DFT calculated oscillator strengths on **1^{Sn}(thf)** and difference electron densities of selected characteristic spin-allowed transitions (isosurface value 0.005 a.u., purple = electron loss, orange = electron gain, CPCM-(THF)-RIJCOSX-B3LYP-D3BJ-ZORA/def2-TZVPP/old-ZORA-TZVPP(Sn)).

a)

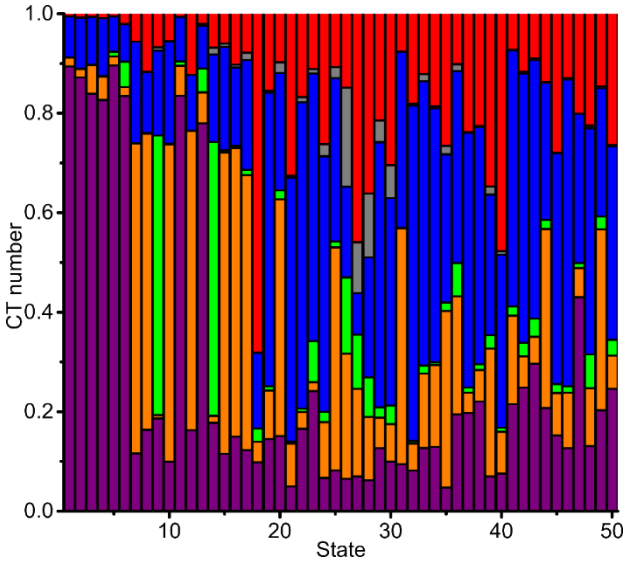

b)

1: 394 nm / 0.0118	2: 364 nm / 0.0113	3: 329 nm / 0.0396	4: 309 nm / 0.0192	5: 305 nm / 0.0194
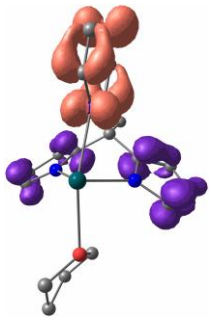	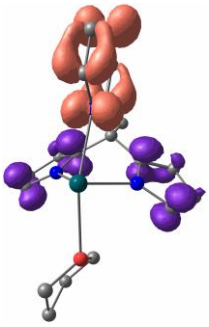	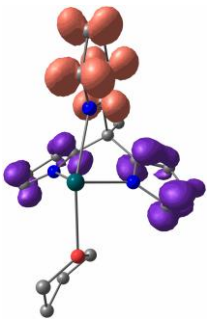	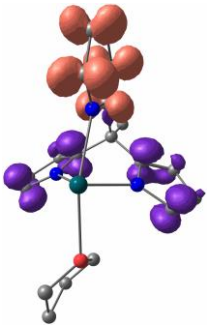	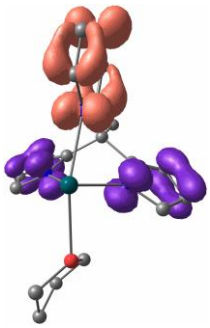
6: 295 nm / 0.00921	7: 289 nm / 0.00404	8: 281 nm / 0.00413	9: 277 nm / 0.000155	10: 271 nm / 0.00149
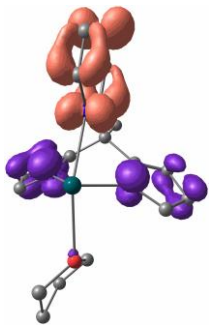	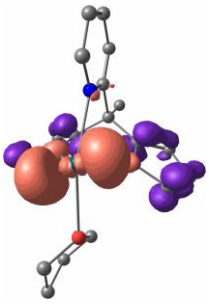	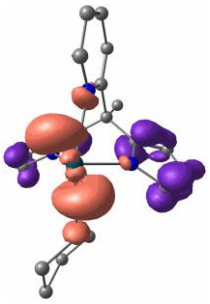	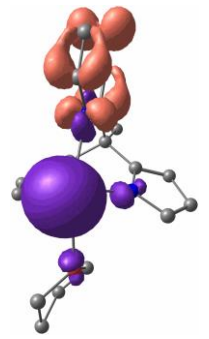	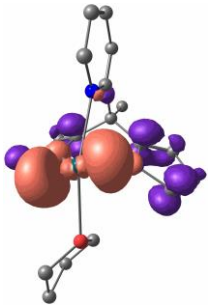
11: 266 nm / 0.00575	12: 263 nm / 0.00156	13: 258 nm / 0.000949	14: 244 nm / 0.00789	15: 240 nm / 0.0104
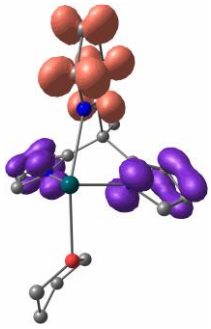	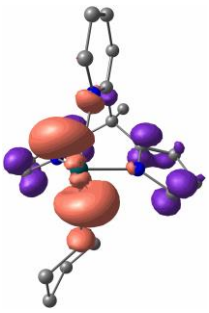	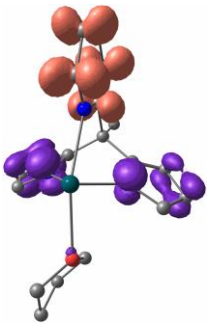	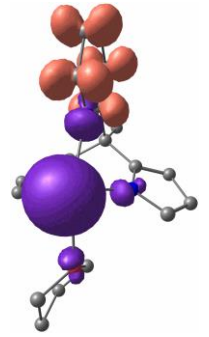	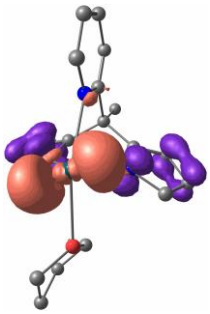
16: 235 nm / 0.0201	17: 232 nm / 0.0236	18: 230 nm / 0.0133	19: 229 nm / 0.0549	20: 227 nm / 0.0540
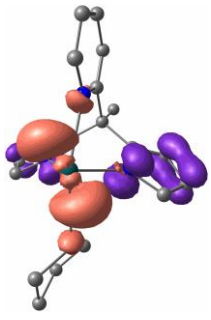	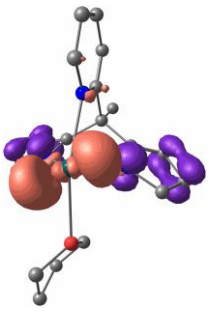	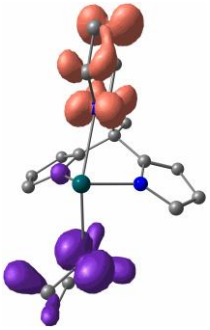	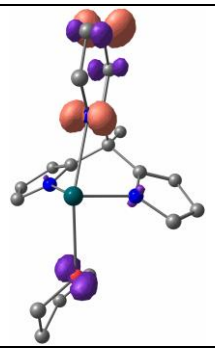	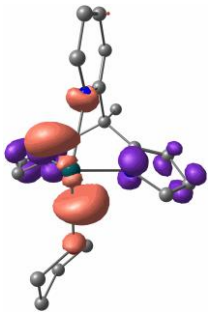

Fig. S30 a) Charge transfer analysis of the 50 lowest spin-allowed transitions of **1^{Sn}(thf)** (green: MLCT, purple: ILCT, orange: LMCT, blue: IL, grey: MC) and b) difference electron densities of the 20 lowest spin-allowed transitions of **1^{Sn}(thf)** with the respective wavelength and oscillator strength (purple = electron loss; orange = electron gain) displayed at an isosurface value of 0.005 a.u..

HOMO−5 / −7.3049	HOMO−4 / −6.6548	HOMO−3 / −6.2530	HOMO−2 / −6.0999	HOMO−1 / −5.4995	HOMO / −5.1976
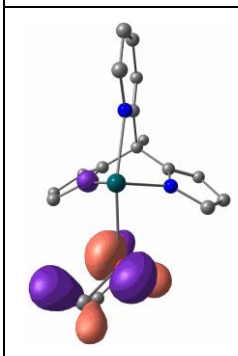	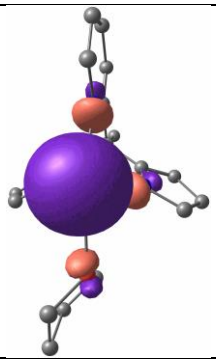	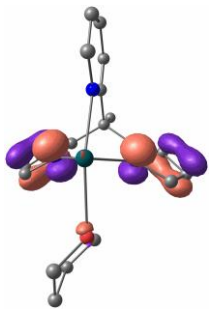	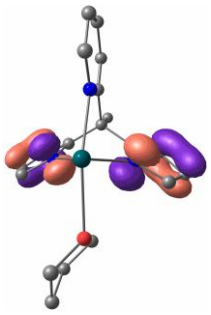	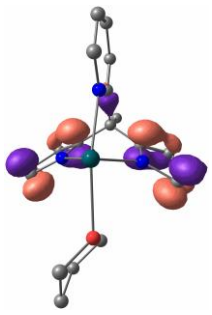	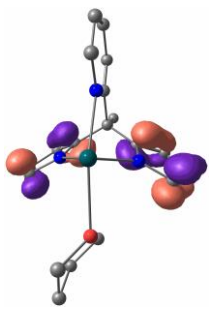
LUMO / −1.4130	LUMO+1 / −0.8115	LUMO+2 / −0.1691	LUMO+3 / −0.0817	LUMO+4 / 0.9350	LUMO+5 / 1.2053
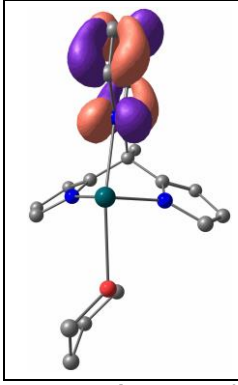	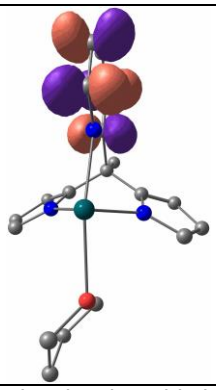	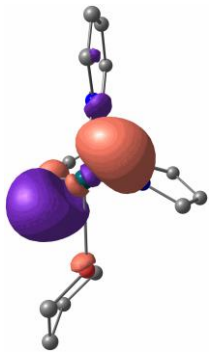	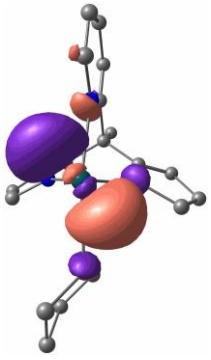	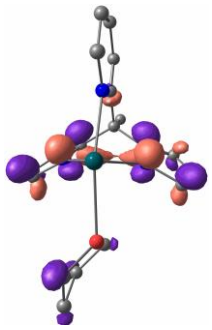	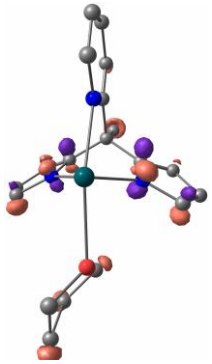

Fig. S31 Selected molecular orbitals of **1^{Sn}(thf)** with energies given in eV, displayed at an isosurface value of 0.07 a.u..

Table S4 Relative Gibbs free energies ΔG_{298} at 298 K of triplet states, ^{1}GS and transition states (TS) in eV, calculated by DFT for **1^{Sn}(thf)**.

^{3}ILCT	0
^{3}LMCT$_{py}$	−0.09
^{3}MLCT	+0.85
^{3}LMCT$_{pyr}$	+0.12
^{1}GS	−2.43

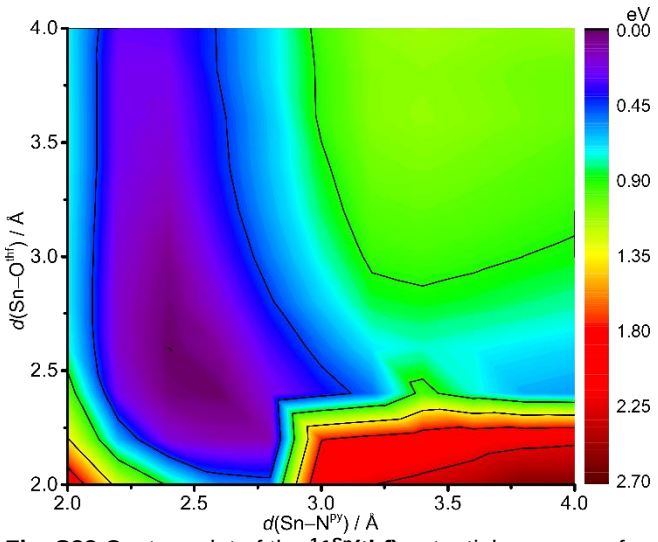

Fig. S32 Contour plot of the **^{1}1^{Sn}(thf)** potential energy surface, according to single-point energies of a 2D relaxed potential energy surface scan as projection along the Sn–N^{py} and Sn–O^{thf} stretching modes on the triplet hypersurface **^{3}1^{Sn}** of **1^{Sn}(thf)** (CPCM-(THF)-RIJCOSX-B3LYP-D3BJ-ZORA/def2-TZVPP/old-ZORA-TZVPP(Sn)).

1 G. Gao, I. Korobkov and S. Gambarotta, *Inorg. Chem.*, 2004, **43**, 1108–1115.
2 M. J. S. Gynane, D. H. Harris, M. F. Lappert, P. P. Power, P. Rivière and M. Rivière-Baudet, *Dalton Trans.*, 1977, 2004–2009.
3 G. R. Fulmer, A. J. M. Miller, N. H. Sherden, H. E. Gottlieb, A. Nudelman, B. M. Stoltz, J. E. Bercaw and K. I. Goldberg, *Organometallics*, 2010, **29**, 2176–2179.
4 F. Barigelletti, D. Sandrini, M. Maestri, V. Balzani, A. von Zelewsky, L. Chassot, P. Jolliet and U. Maeder, *Inorg. Chem.*, 1988, **27**, 3644–3647.
5 G. D. Hager and G. A. Crosby, *J. Am. Chem. Soc.*, 1975, **97**, 7031–7037.
6 F. Neese, *WIREs Comput. Mol. Sci.*, 2012, **2**, 73–78.
7 F. Neese, *WIREs Comput. Mol. Sci.*, 2022, **12**, e1606.
8 Chengteh Lee, Weitao Yang and R. G. Parr, *Phys. Rev. B*, 1988, **37**, 785–789.
9 B. Miehlich, A. Savin, H. Stoll and H. Preuss, *Chem. Phys. Lett.*, 1989, **157**, 200–206.
10 A. D. Becke, *J. Chem. Phys.*, 1993, **98**, 5648–5652.
11 F. Weigend and R. Ahlrichs, *Phys. Chem. Chem. Phys.*, 2005, **7**, 3297–3305.
12 F. Weigend, *Phys. Chem. Chem. Phys.*, 2006, **8**, 1057–1065.
13 D. A. Pantazis and F. Neese, *J. Chem. Theory Comput.*, 2009, **5**, 2229–2238.
14 D. A. Pantazis, X.-Y. Chen, C. R. Landis and F. Neese, *J. Chem. Theory Comput.*, 2008, **4**, 908–919.
15 D. A. Pantazis and F. Neese, *Theor. Chem. Acc.*, 2012, **131**, 1292.
16 D. A. Pantazis and F. Neese, *J. Chem. Theory Comput.*, 2011, **7**, 677–684.
17 F. Neese, F. Wennmohs, A. Hansen and U. Becker, *Chem. Phys.*, 2009, **356**, 98–109.
18 R. Izsák and F. Neese, *J. Chem. Phys.*, 2011, **135**, 144105.
19 C. van Wüllen, *J. Chem. Phys.*, 1998, **109**, 392–399.
20 E. van Lenthe, E. J. Baerends and J. G. Snijders, *J. Chem. Phys.*, 1993, **99**, 4597–4610.
21 S. Miertus, E. Scrocco and J. Tomasi, *Chem. Phys.*, 1981, **55**, 117–129.
22 V. Barone and M. Cossi, *J. Phys. Chem. A*, 1998, **102**, 1995–2001.
23 S. Grimme, J. Antony, S. Ehrlich and H. Krieg, *J. Chem. Phys.*, 2010, **132**, 154104 1-19.
24 S. Grimme, S. Ehrlich and L. Goerigk, *J. Comput. Chem.*, 2011, **32**, 1456–1465.
25 F. Plasser, *J. Chem. Phys.*, 2020, **152**, 84108.
26 *STOE & Cie, X-Area*, STOE & Cie GmbH, Darmstadt, Germany.
27 G. M. Sheldrick, *Acta Crystallogr., Sect. A*, 2015, **71**, 3–8.
28 G. M. Sheldrick, *Acta Crystallogr., Sect. C*, 2015, **71**, 3–8.
29 G. M. Sheldrick, *Acta Crystallogr., Sect. A*, 2008, **64**, 112–122.
30 C. B. Hübschle, G. M. Sheldrick and B. Dittrich, *J. Appl. Crystallogr.*, 2011, **44**, 1281–1284.